



Microstructural parameters affecting creep induced load shedding in Ti-6242 by a size dependent crystal plasticity FE model

Gayathri Venkataramani, Kedar Kirane, Somnath Ghosh*

*Department of Mechanical Engineering, The Ohio State University, Room W496, Scott Laboratory,
201 West 19th Avenue, Columbus, OH 43210, USA*

Received 1 February 2007; received in final revised form 25 April 2007
Available online 23 May 2007

Abstract

This paper is aimed at identifying critical microstructural parameters that cause local stress concentration due to load shedding between microstructural regions of varying strengths. This stress is viewed as one of the fundamental reasons for crack initiation in Ti-6242. A rate dependent, anisotropic, elasto-crystal plasticity based finite element model (CPFEM) for poly-phase Ti-6242 is used in this study to identify the critical variables responsible for localized stress concentration due to load shedding. The model can account for various microstructural features like grain size, orientation and misorientation distributions. Various microstructural variables, such as crystal orientation, misorientation, grain size, Schmid factor and composition of phases, are considered in a detailed parametric study. Critical combinations of these parameters that result in high stress due to load shedding are identified. Finally, load shedding in a microstructure model of polycrystalline Ti-6242 is discussed from the results of CPFEM simulations. The model is statistically equivalent with respect to features observed in OIM scans.

© 2007 Elsevier Ltd. All rights reserved.

Keywords: Crystal plasticity; Finite elements; Ti-6242; Grain size effect; Sensitivity analysis

* Corresponding author. Tel.: +1 614 292 2599; fax: +1 614 292 3163.
E-mail address: ghosh.5@osu.edu (S. Ghosh).

1. Introduction

Alpha and near alpha titanium alloys are known for their high specific strength, good corrosion resistance, relatively low density and high fracture toughness. Due to these superior mechanical properties they are used in several high performance applications ranging from the aerospace structural components to the orthopedic, dental and sporting goods (Froes, 1998). One such two-phase alloy is Ti–6Al–2Sn–4Zr–2Mo (Ti-6242), which is used in the compressor rotor of aircraft engines. The composition of Ti-6242 is given in Table 1. Prior research by Chu (1970), Imam and Gilmore (1979), Miller et al. (1987), Odegard and Thompson (1974) have shown that the alloy creeps at room temperature and also at fraction of the macroscopic yield stress. This results in marked reduction or ‘debit’ in number of cycles to failure when subjected to dwell fatigue in comparison with pure fatigue specimens (Sinha et al., 2004). In dwell loading, the load is periodically ramped to a certain level, held at that level for finite time and subsequently reduced to zero. The study of creep and dwell fatigue of Ti-6242 has drawn significant research attention.

Orientation imaging microscopy (OIM) scans of the failure sites in Ti-6242 samples subjected to dwell fatigue and creep have shown that failure sites are faceted and have a near basal orientation (Bache, 2003; Sinha et al., 2006). The faceted nature of the cracks suggests that stress could be a predominant factor in fatigue failure of Ti-6242. This is also confirmed by numerical simulations of creep and dwell fatigue experiments on polycrystalline Ti-6242, explained in Venkataramani et al. (2006). In this paper, a comparison of local stress and strain values corresponding to failure time in creep and dwell has established that local stresses for the two cases are within 2% of each other, while the corresponding strain values differ by 15%. Earlier experiments employing electron back scattered diffraction (EBSD) technique in scanning electron microscopy or orientation imaging microscopy (Sinha et al., 2006) have shown that the relative strength of neighboring grains are highly dependent on the orientation of basal planes with respect to the axis of loading. Large local stress concentrations are found to develop in $\langle c + a \rangle$ oriented grains due to local load shedding from neighboring softer $\langle a \rangle$ oriented grains. Hence the local grain crystallography, leading to load shedding between grains, is of considerable importance in crack initiation in Ti alloys that needs to be studied in detail (Deka et al., 2006; Goh et al., 2003). Local load shedding is attributed to strength mismatch between grain, which in turn is the result of differences in crystal orientation, grain size and Schmid factor. The influence of these microstructural parameters on mechanical response in the computational simulations can be used to establish realistic microstructure–property relations for materials.

To incorporate the effect of various microstructural parameters, a size and time dependent large strain finite element model has been developed in Hasija et al. (2003) and Deka et al. (2006). As shown in the optical micrograph of Fig. 1a, a forged α/β Ti-6242 microstructure consists of transformed β colonies in a matrix of equiaxed primary α grains. The model incorporates rate dependent anisotropic elastic–crystal plasticity constitutive mod-

Table 1
Chemical composition of Ti-6242

Alloy	Al (wt%)	Mo (wt%)	Sn (wt%)	Zr (wt%)	Si (wt%)	O (wt%)	N (wt%)	Ti (wt%)
Ti-6242	6.01	1.96	1.96	4.01	0.10	0.131	0.012	85.82

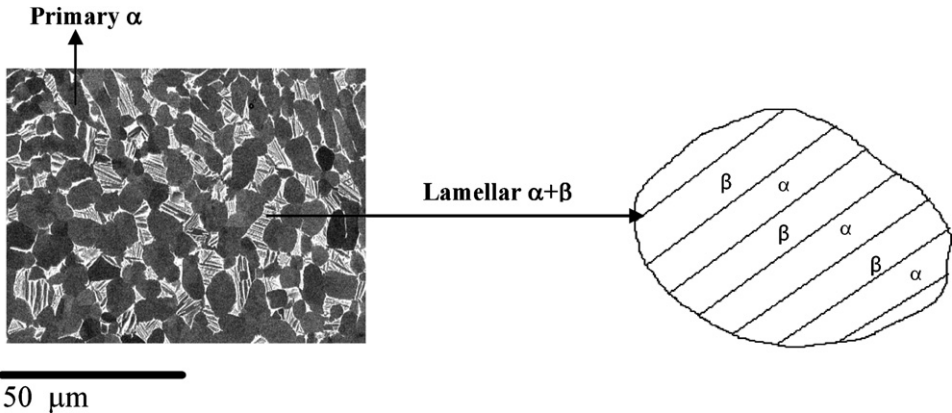


Fig. 1. (a) Microstructure of a forged $\alpha + \beta$ Ti-6242 alloy consisting of transformed β (light phase) colonies in a matrix of equiaxed primary α grains (dark phase). (b) Schematic of a constituent transformed β colony.

els for the different phases in this material. Details of the microstructural morphology are accounted for in the model through accurate phase volume fractions and orientation distributions that are statistically equivalent to those observed in OIM scans. Material properties for each constituent phase and individual slip systems in the crystal plasticity model are calibrated from results of constant strain rate and creep tests with single colony and single crystal specimens by a genetic algorithm based optimization scheme. In addition, tension–compression asymmetry is also incorporated in the slip system variables to reflect experimental observations (Neeraj et al., 2005). A homogenized model of the $\alpha + \beta$ phase colony regions in the Ti-6242 microstructure have been developed in Deka et al. (2006) for incorporation in the CPFEM model of the transformed β phase. Furthermore, polycrystalline specimens show a strong effect of grain size on the flow stress. To account for this effect, a Hall–Petch (Hall, 1951; Petch, 1953) type relation is proposed for size dependent deformation resistance with various characteristic length scales, depending on the slip direction. Parameters in the size dependent yield stress relationship for independent slip systems are determined from single colony and single crystal experiments. The computational model is validated by comparing the results of simulation with those from constant strain rate and creep experiments on Ti-6242 specimens.

The computational model of polycrystalline Ti-6242 with experimentally validated constitutive model is developed to account for various microstructural parameters like texture and grain size. Simulations with this model are used to understand the role of microstructure on the phenomenon of creep induced load shedding. This has been proposed as one of the fundamental reasons for dwell fatigue crack nucleation. Four different microstructural parameters, viz. orientation, misorientation between grains, Schmid factor and grain size are investigated. Experiments in Neeraj et al. (2005) have also shown that the creep response of Ti-6242 has a considerable dependence on proportion of constituent primary α and transformed β phases. A study on the effect of volume fraction of primary α and transformed β phases on the macroscopic and creep response of polycrystalline Ti-6242 is undertaken. Finally, a 3D polycrystalline model is simulated as a statistical equivalent of a real Ti-6242 microstructure. The simulated model is generated by a constrained Voronoi tessellation method, in which experimentally observed microstructural distributions of

grain shape, size, orientation and misorientation are used for providing constraints to the tessellation process. Finite element analysis of this microstructural model is conducted to probe into the influence of various microstructural features on local stress risers. Observations of this study may be used for development of failure initiation criterion.

2. Material description

An optical micrograph of a forged α/β Ti-6242 material is shown in Fig. 1a. The microstructure consists of regions of transformed β colonies in a matrix of equiaxed primary α grains with an hcp crystalline structure. The transformed β colonies consist of alternating α (hcp) and β (bcc) laths as shown in Fig. 1b. For hcp lattice structure, the material basis vectors are denoted by a set of non-orthogonal base vectors, $\{\mathbf{a}_1, \mathbf{a}_2, \mathbf{a}_3, \mathbf{c}\}$ as discussed in Hasija et al. (2003). As shown in Fig. 2a, the hcp crystals consist of five different families of slip systems, namely the basal $\langle \mathbf{a} \rangle$, prismatic $\langle \mathbf{a} \rangle$, pyramidal $\langle \mathbf{a} \rangle$, first order pyramidal $\langle \mathbf{c} + \mathbf{a} \rangle$ and second order pyramidal $\langle \mathbf{c} + \mathbf{a} \rangle$ with a total of 30 possible slip systems. A transversely isotropic elastic response is assumed for these crystals with five independent constants. The bcc crystal system consist of three different slip families, $\langle 111 \rangle \{110\}$, $\langle 111 \rangle \{112\}$ and $\langle 111 \rangle \{123\}$ with a total of 48 slip systems as shown in Fig. 2b. A cubic symmetric elastic matrix is assumed for the bcc material with three independent constants. For the specimens analyzed, the volume fraction of the transformed β phase in the Ti-6242 material microstructure is 30%. Within the transformed β colonies, the α and β lamellae are experimentally observed (Savage, 2000) to have volume fractions of approximately 88% and 12% respectively. The orientations of α and β lamellae follow a Burger's orientation relationship that is expressed as $(101)_\beta \parallel (0001)_\alpha$, $[1\bar{1}\bar{1}]_\beta \parallel [2\bar{1}\bar{1}0]_\alpha$. This relation brings the hcp \mathbf{a}_1 ($[2\bar{1}\bar{1}0]$) slip direction in alignment with the bcc \mathbf{b}_1 slip direction (Suri et al., 1999).

3. The constitutive model

3.1. Crystal plasticity based material model

The deformation behavior of individual phases of the Ti-6242 microstructure is modeled using a rate dependent, isothermal, elastic–plastic, finite strain, crystal plasticity formulation, following Kalidindi et al. (1992). Twinning is not accounted for in the model since the Al content in Ti-6242 is rather high, $\sim 6.01\%$. Experimentally it has been observed in Williams et al. (2002), that twinning occurs in Ti alloys only for low Al content. The general framework for the crystal plasticity formulation is taken to be the same for both the hcp and bcc phases, with the only difference introduced in the hardening laws. The stress–strain relation in this model is written in terms of the second Piola–Kirchoff stress \mathbf{S} ($= \det \mathbf{F}^e \mathbf{F}^{e-1} \boldsymbol{\sigma} \mathbf{F}^{e-T}$) and the work conjugate Lagrange Green strain tensor \mathbf{E}^e ($= \frac{1}{2} \{\mathbf{F}^{eT} \mathbf{F}^e - \mathbf{I}\}$) as

$$\mathbf{S} = \mathbf{C} : \mathbf{E}^e \quad (1)$$

where \mathbf{C} is the fourth order anisotropic elasticity tensor, $\boldsymbol{\sigma}$ is the Cauchy stress tensor and \mathbf{F}^e is the elastic deformation gradient defined by the relation

$$\mathbf{F}^e \equiv \mathbf{F} \mathbf{F}^{-p}, \quad \det \mathbf{F}^e > 0 \quad (2)$$

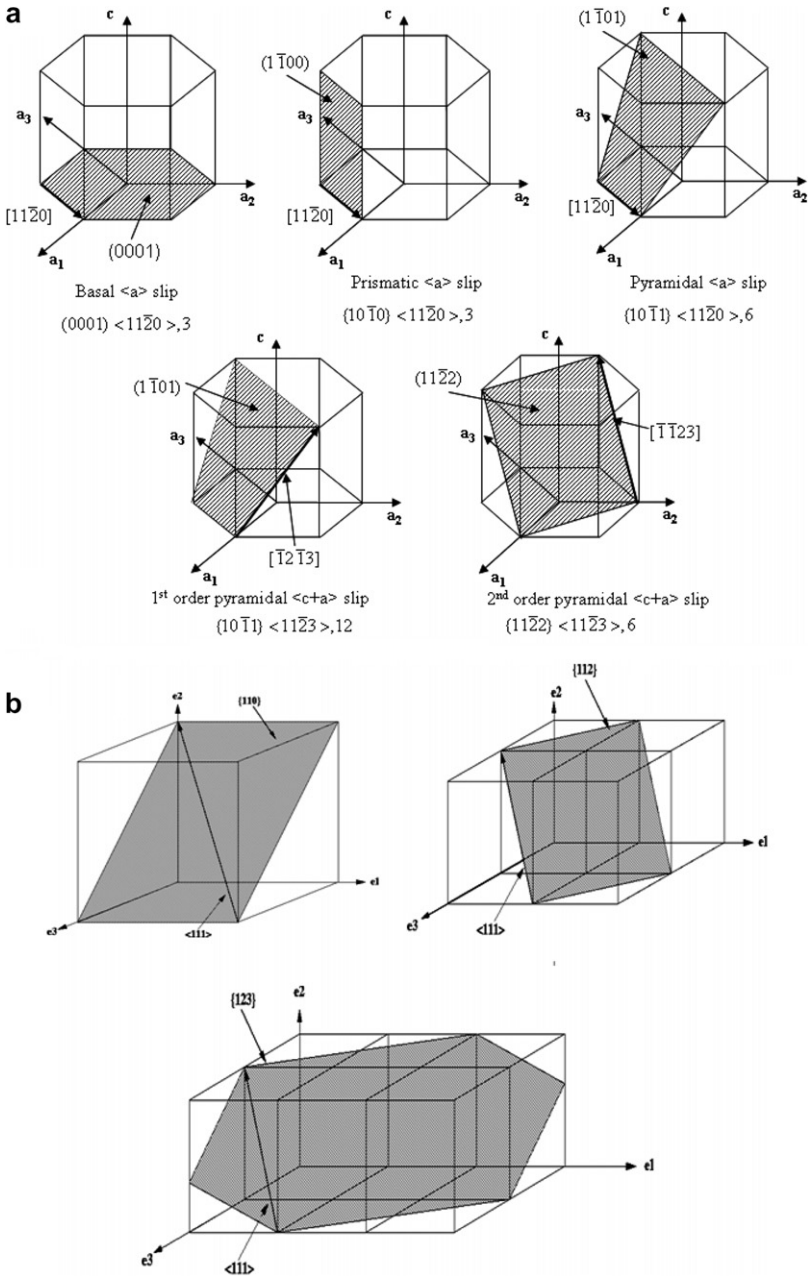


Fig. 2. Schematic diagrams showing (a) the non-orthogonal basis and slip systems in a hcp crystal and (b) the orthogonal basis and slip systems in bcc crystals.

\mathbf{F} and \mathbf{F}^p are the deformation gradient and its plastic component respectively with the incompressibility constraint $\det \mathbf{F}^p = 1$. The crystallographic orientation in each grain evolves with deformation that is accounted for through the relation. $\mathbf{m}^\alpha(t) = \mathbf{F}^e(t) \mathbf{m}_0^\alpha$,

$\mathbf{n}^\alpha(t) = \mathbf{F}^{e-T}(t)\mathbf{n}_0^\alpha$. The flow rule governing evolution of plastic deformation is expressed in terms of the plastic velocity gradient as

$$\mathbf{L}^p = \dot{\mathbf{F}}^p \mathbf{F}^{p-1} = \sum_\alpha \dot{\gamma}^\alpha s_0^\alpha \tag{3}$$

where the α th slip system Schmid tensor is expressed as $s_0^\alpha \equiv m_0^\alpha \otimes n_0^\alpha$ in terms of the slip direction m_0^α and slip plane normal n_0^α in the reference configuration. The plastic shearing rate $\dot{\gamma}^\alpha$ on the α th slip system is given by the power law relation (Kalidindi et al., 1992) expressed as

$$\dot{\gamma}^\alpha = \tilde{\gamma} \left| \frac{\tau^\alpha}{g^\alpha} \right|^{1/m} \text{sign}(\tau^\alpha), \quad \tau^\alpha \equiv (\mathbf{C}^e : \mathbf{S}) \cdot \mathbf{s}^{\alpha} \tag{4}$$

Here $\tilde{\gamma}$ is the reference plastic shearing rate, τ^α and g^α are the α th slip system resolved shear stress and the slip system deformation resistance respectively, m is the material rate sensitivity parameter and \mathbf{C}^e is the elastic stretch. The slip system resistance is taken to evolve as

$$\dot{g}^\alpha = \sum_{\beta=1}^{n_{slip}} h^{\alpha\beta} |\dot{\gamma}^\beta| = \sum_{\beta} q^{\alpha\beta} h^\beta |\dot{\gamma}^\beta| \tag{5}$$

where $h^{\alpha\beta}$ corresponds to the strain hardening rate due to self and latent hardening, h^β is self-hardening rate and $q^{\alpha\beta}$ is a matrix describing the latent hardening. For the hcp phase the evolution of the self-hardening rate, is governed by the relation given in Kothari and Anand (1998):

$$h^\beta = h_0^\beta \left| 1 - \frac{g^\beta}{g_s^\beta} \right|^r \text{sign} \left(1 - \frac{g^\beta}{g_s^\beta} \right), \quad g_s^\beta = \tilde{g} \left| \frac{\dot{\gamma}^\beta}{\tilde{\gamma}} \right|^n \tag{6}$$

where h_0^β is the initial hardening rate, g_s^β is the saturation slip deformation resistance, g^β and r , \tilde{g} and n are the slip system hardening parameters. It should be noted that a negative sign for h^β in Eq. (6) results when g^β exceeds its saturation value g_s^β . From Eq. (5), this causes a reduction in g^β to bring it back to below the saturation value. For bcc materials, the evolution of the self-hardening rate is given in Harren et al. (1989) as

$$h^\beta = h_s^\beta + \text{sech}^2 \left[\left(\frac{h_0^\beta - h_s^\beta}{\tau_s^\beta - \tau_0^\beta} \right) \gamma_a \right] (h_0^\beta - h_s^\beta), \quad \gamma_a = \int_0^t \sum_{\beta=1}^{n_{slip}} |\dot{\gamma}^\beta| \tag{7}$$

where h_0^β and h_s^β are the initial and asymptotic hardening rates, τ_s^β represents the saturation value of the shear stress when $h_s^\beta = 0$, and γ_a is a measure of total plastic shear. For modeling cyclic deformation it is important to include kinematic hardening. This is done by including a backstress in the power law Eq. (4) as in Hasija et al. (2003). Consequently, the rate of crystallographic slip on a given slip system is expressed as

$$\dot{\gamma}^{(\alpha)} = \dot{\gamma}_0 \left| \frac{\tau^{(\alpha)} - \chi^{(\alpha)}}{g^{(\alpha)}} \right|^{1/m} \text{sign}(\tau^{(\alpha)} - \chi^{(\alpha)}) \tag{8}$$

where $\chi^{(\alpha)}$ is the backstress on the α th slip system. An Armstrong–Frederick type nonlinear kinematic hardening rule is chosen for the evolution of backstress as

$$\dot{\chi}^{(\alpha)} = c\dot{\gamma}^{(\alpha)} - d\chi^{(\alpha)}|\dot{\gamma}^{(\alpha)}| \quad (9)$$

Here c and d are the direct hardening and the dynamic recovery coefficients respectively.

3.2. Size dependence in the crystal plasticity model for Ti-6242

Experiments on single colony α/β Ti 6242 and single crystal α (Ti-6Al-4V) have been used in Hasija et al. (2003) and Deka et al. (2006) to calibrate crystal plasticity parameters for individual slip systems in each of the constituent phases by a genetic algorithm based optimization scheme. The calibrated values of the initial slip system deformation resistance g^{α} reflect the anisotropy exhibited by the three basal and prism slip systems and also the asymmetry between the tension and compression observed in the single colonies of α/β Ti-6242. The tension/compression asymmetry has been attributed to one or a combination of a number of mechanisms, viz. residual stresses in single colony due to growth process, elastic stress fields at the α/β interface aiding or impairing slip transmission, effects on the mobility of $\langle a \rangle$ type dislocations in the α phase, and effects on the mobility of dislocations in the β phase and differing slip transmission mechanisms based on the direction of loading (Savage, 2000). Tension–compression asymmetry is incorporated in the crystal plasticity model by using different values of critical resolved shear stress on slip system, corresponding to positive and negative signs of the maximum principal stress at a point.

The size scales of α and β laths in single colonies are approximately an order of magnitude greater than the respective in situ grain sizes in polycrystalline Ti-6242. It has been inferred in Deka et al. (2006) that significant difference is observed in the results of simulation and experiments if the material parameters calibrated from single colony and single experiments are directly used to predict the mechanical response of polycrystalline Ti-6242. This is because the polycrystalline sample exhibits a strong flow stress dependence on the grain size. Strengthening with smaller lath size in β processed Ti-6Al-4V has also been experimentally observed in Norfleet (2005). To account for size effects in the crystal plasticity model for polycrystalline Ti-6242, parameters calibrated from single crystal (primary α) and single colony (transformed β) tests were adjusted in an ad hoc manner in Deka et al. (2006) to match experimental stress–strain plots. This paper incorporates a more physical grain size effect in the model. It should be emphasized that the size dependence is incorporated in the initial value of the slip deformation resistance g_0^{α} . Subsequent evolution of g^{α} occurs according to Eq. (5). In crystal plasticity formulation, an equation that relates the slip system initial deformation resistance g_0^{α} to a characteristic size can be expressed by the Hall–Petch relationship (Hall, 1951; Petch, 1953) as

$$g_0^{\alpha} = \bar{g}_0^{\alpha} + \frac{K^{\alpha}}{\sqrt{D^{\alpha}}} \quad (10)$$

where \bar{g}_0^{α} and K^{α} are slip system size effect constants that refer to the interior slip system deformation resistance and slope respectively, and D^{α} is the characteristic length scale governing size effect. For multi-phase materials such as Ti-6242, the grain size, colony size, and α and β lath thicknesses in the colony can all serve as different characteristic length scales governing size effect. The ease of α/β slip transmission for \mathbf{a}_1 , \mathbf{a}_2 and \mathbf{a}_3 basal and prismatic slips in the transformed β region varies significantly due to varying misalignment between the corresponding slips in α and β phase. This causes anisotropy in the slip system initial deformation resistance g_0^{α} .

In the transformed β regions, three different characteristic length scales are considered. These are the colony size D_c , the α lath thickness l_α and the β lath thickness l_β . The plastic deformation is activated through two types of slip modes, namely the hard and soft slip modes, as illustrated in Fig. 3a and b respectively. The orientations of α and β lamellae follow the Burger's orientation relationship, which brings the hcp a_1 ($[2\bar{1}\bar{1}0]$) slip direction into coincidence with the bcc b_1 slip resulting in a relatively easy slip transmission across the interface. Two types of slip modes, viz. a soft and a hard slip mode are defined in this context. The soft slip mode corresponds to systems in which dislocations glide parallel to the interface and transmit freely across the α/β interface due to the presence of common slip system between the two phases. The a_1 slip direction of the basal and prism and b_1 slip direction of bcc may be classified as soft slip modes. The resistance to slip in the soft slip mode is only from the colony boundary and hence the colony size D_c is the characteristic length for the size effect. The hard slip mode, on the other hand, corresponds to systems in which the slip transmission is impeded by the α/β interface due to the absence of a common slip system between the α and β phases. There is a significant misalignment between the α phase a_2 ($[\bar{1}2\bar{1}0]$) and β phase b_2 slip directions, and also between the a_3 ($[\bar{1}\bar{1}20]$) and all $\langle 111 \rangle_\beta$ directions in the β phase. Consequently, the barrier to dislocation motion across the interface is sufficiently large that dislocation pile-ups are developed for these slips. Hence, these are classified as hard slip modes. Correspondingly in the β phase, slip directions other than b_1 ($[\bar{1}11]$), are expected to be impeded by lath boundary and are classified as hard slip modes. Thus the characteristic lengths for systems with hard slip modes are l_α and l_β for the hcp and bcc phases respectively. In the case of primary α region, the grain boundary retards the transmission of slip for all systems. These systems correspond to soft slip modes with the grain size D_g as the characteristic length. Characteristic lengths used in the size effect relationship are summarized in Table 2.

The internal grain strength \bar{g}_0^z in Eq. (10) may be obtained from the initial g_0^z values calibrated from single crystal and single colony experiments in Deka et al. (2006) for primary α and transformed β regions respectively. While slip system deformation resistance \bar{g}_0^z may be same for some slip systems, anisotropy is still observed in their strength due to different values in the second term in Eq. (10), arising out of dislocation pile-up at the lath

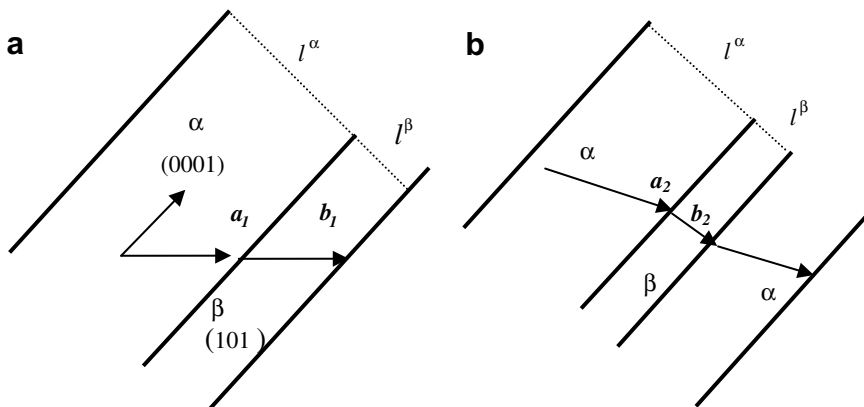


Fig. 3. Slip modes at α/β interface in transformed β phase of Ti-6242: (a) Soft slip mode showing presence of common slip a_1 and b_1 . (b) Hard slip mode showing large misorientation between a_2 and b_2 .

Table 2

Grain size and lath size of single colony and polycrystalline experimental samples

l_α (single colony)	10 μm
l_β (single colony)	2 μm
l_α (polycrystal)	1 μm
l_β (polycrystal)	0.35 μm
$D_g = D_c$	5 μm

boundary. The constants K_h^α or K_s^α corresponding to the Hall–Petch slope of the $g_0^\alpha - \frac{1}{\sqrt{D^\alpha}}$ plot is based on dislocation pile-up model for hard and soft slip modes. In the primary α and transformed β regions, the expression for the Hall–Petch slope K_s^α corresponding to soft slip modes is given in Cao et al. (2000), Li and Chou (1970) as

$$K_s^\alpha = \sqrt{\frac{(2-v)\pi\tau^*Gb}{2(1-v)}} \quad (11)$$

where v is the Poisson ratio, G is the shear modulus, b is the Burger vector and τ^* is the barrier strength for grain boundary. The value of τ^* is estimated approximately as $0.01G$ in the literature (Semiatin and Bieler, 2001; Cao et al., 2000) for the soft slip mode. Values of various constants are summarized in Table 3. For the hard slip mode, the value of slope K_h^α is based on expression for strengthening due to dislocation pile-ups at the interface as developed by Eshelby (1963), Semiatin and Bieler (2001) and is given as

$$K_h^\alpha = \sqrt{\frac{4\tau^*Gb}{\alpha\pi}} \quad (12)$$

where α is a constant taken as 1.0 for screw dislocations and $(1-v)$ for edge dislocations. In the present study, the screw and edge dislocations are taken to be 50% each, and hence $\alpha = \frac{1}{2}[1 + (1-v)]$. The g^α values calibrated for the hard slip modes from single colony experiments, reflect the effect of strengthening due to lath boundaries. The slope K_h^α for the hard slip mode is obtained by substituting in Eq. (10), the g_0^α value of that slip mode calibrated from single colony experiments, the \bar{g}_0^α obtained for the a_1 basal system (which shows no strengthening due to lath boundaries) and the l_α of hcp phase. The barrier strength τ^* for the hard slip mode is obtained by substituting the calculated value of K_h^α in Eq. (12). The barrier strength τ^* for soft deformation is assumed as $0.01G$, from which the constant K_s^α can be obtained for different systems in tension and compression. For slip systems with identical \bar{g}_0^α , different slopes K_h^α and K_s^α in the Hall–Petch relation give rise to anisotropy in the slip system deformation values. For the other bcc phase slip systems that

Table 3

Values of constants used in the determination of K_h^α and K_s^α in the Hall–Petch relations

G (primary α)	48.0 GPa
G (transformed β – hcp)	43.0 GPa
G (transformed β – bcc)	115.0 GPa
b (hcp)	0.30 nm
b (bcc)	0.33 nm
v	0.33
α	0.835

have resistance from the lath boundary, a barrier strength of $0.015G$ is assumed to determine K_h^z . For the primary α phase since there is no resistance to slip due to the grain boundary. Consequently, calibrated values of g_0^z for individual systems in the compression experiments of [Deka et al. \(2006\)](#) directly yield the \bar{g}_0^z values of Eq. (10). With known values of \bar{g}_0^z and K_s^z from Eq. (11), the g_0^z value for any grain size can be obtained by using the Hall–Petch relationship of Eq. (10). Hall–Petch parameters, derived for tension and compression are provided in [Tables 4 and 5](#) respectively.

Finally, it has been shown by [Maruyama et al. \(2001\)](#) that the Hall–Petch relationship for lamellar structures reaches a saturation value at a critical lamellar spacing that is explained by the pile-up model of dislocations at lamellar interfaces. The critical lamellar spacing λ^* , below which there is no further strengthening, is given as [Maruyama et al. \(2001\)](#)

$$\lambda^* = \frac{Gb}{(1-\nu)\tau^*} \quad (13)$$

This limiting value λ^* is incorporated for the characteristic lath thicknesses l_α and l_β to calculate the saturation g^z values.

3.3. An equivalent homogenized model for transformed β

In the modeling of polycrystalline Ti-6242, each element in the CPFEM model represents a sub-region of a single phase of the primary α -transformed β grain microstructure. It is computationally exhaustive to explicitly model alternating laths of $\alpha - \beta$ phases in the model of the transformed β colonies as shown in [Fig. 1a](#). Consequently, a homogenized equivalent crystal model of the $\alpha + \beta$ transformed β phase colony regions has been developed in [Deka et al. \(2006\)](#). The model consists of 78 slip systems, of which 30 correspond to hcp (secondary α) and 48 correspond to bcc slip systems. The relative orientations of the slip systems follow the alignment of α and β lamellae as required by the Burger's orientation relationship. The equivalent crystal is constructed based on the assumptions of the Taylor model, where a uniform deformation gradient F_{ij} is assumed for the two phases. In [Deka et al. \(2006\)](#), the equivalent transformed β model has been shown to yield reasonably accurate predictions of the overall stress–strain behavior and slip system evolution, in comparison with a detailed FE model containing explicit representation of the α and β

Table 4

Values of Hall–Petch constants (g_0 and K) and g^z of hcp slip systems in polycrystalline Ti-6242 in tension obtained from size effect relationship

	a_1 basal	a_2 basal	a_3 basal	a_1 prism	a_2 prism	a_3 prism
<i>Primary α</i>						
g_0	284.0	284.0	284.0	282.2	282.2	282.2
K	164.5	164.5	164.5	164.5	164.5	164.5
g^z	357.6	357.6	357.6	355.8	355.8	355.8
<i>Transformed β/hcp</i>						
g_0	284.0	284.0	284.0	240.0	240.0	240.0
K	147.4	98.0	98.0	147.4	15.8	47.4
g^z	349.9	382.0	382.0	305.9	255.8	287.4

Table 5

Values of Hall–Petch constants (g_0 and K) and g^z of hcp slip systems in polycrystalline Ti-6242 in compression, obtained from size effect relationship

	a_1 basal	a_2 basal	a_3 basal	a_1 prism	a_2 prism	a_3 prism
<i>Primary α</i>						
g_0	322.0	322.0	322.0	320.0	320.0	320.0
K	164.5	164.5	164.5	164.5	164.5	164.5
g^z	395.6	395.6	395.6	393.6	393.6	393.6
<i>Transformed β/hcp</i>						
g_0	385.0	385.0	385.0	382.6	382.6	382.6
K	147.4	189.7	205.5	147.4	188.5	204.3
g^z	450.9	574.7	590.6	448.5	571.1	586.9

phases. The equivalent model is compact, and is hence convenient to use for representing the transformed β phase in a FE model of Ti-6242.

3.4. Validation of the Ti-6242 model for constant strain rate and creep tests

The crystal plasticity model is incorporated in the commercial finite element code **MSC MARC (2005)** using the user defined material routine HYPELA2. An implicit time integration scheme proposed in **Kalidindi et al. (1992)** has been employed to integrate the crystal plasticity Eqs. (1)–(9). Known deformation variables like the deformation gradient $\mathbf{F}(t)$, the plastic deformation gradient $\mathbf{F}^P(t)$, and the slip system deformation resistance $s^\alpha(t)$ at time t , and the deformation gradient $\mathbf{F}(t + \Delta t)$ at $t + \Delta t$ are passed to the material update routine in HYPELA2. The integration algorithm in the HYPELA2 subroutine

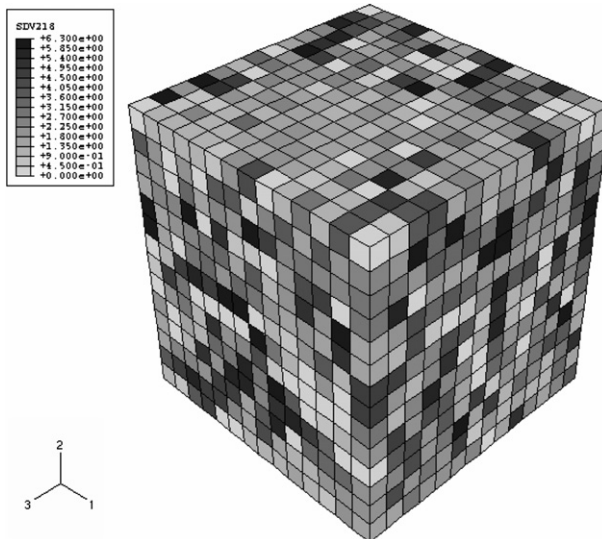


Fig. 4. Finite element mesh with statistically equivalent orientation distribution showing the contour of orientation distribution (radians) in the FE model of polycrystalline Ti-6242.

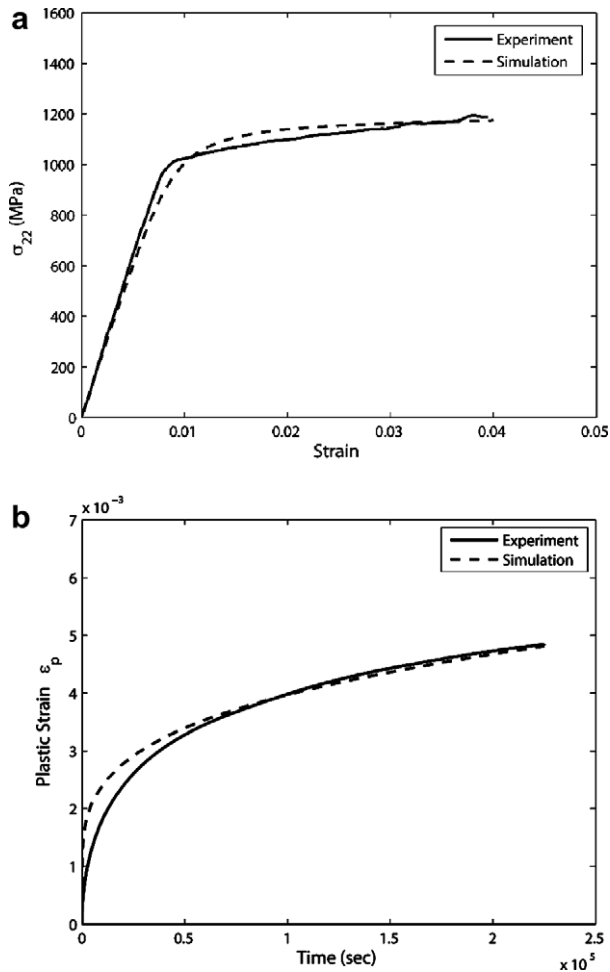


Fig. 5. Validating the Ti-6242 computational model with experimental results: (a) Stress–strain plots for compression test with constant strain rate = $1 \times 10^{-4} \text{ s}^{-1}$ and (b) evolution of plastic strain for compression creep at a stress level of 907 MPa.

updates stresses, plastic strains, and all slip system internal variables to the end of the time step at $t + \Delta t$.

Simulations of two types of mechanical tests, namely (i) constant strain rate test in compression at imposed strain rate of $1 \times 10^{-4} \text{ s}^{-1}$, and (ii) compressive creep tests at 95.5% of the yield stress or 907 MPa, are conducted with the size dependent crystal plasticity model. The results of the simulations are compared with those from experiments on polycrystalline Ti-6242 in Neeraj et al. (2005) and Savage (2000). The FE model of the polycrystalline aggregate consists of a unit cubic domain that is discretized into 2744 eight-noded tri-linear brick elements in the commercial finite element code MARC. Each element in the FE representation of polycrystalline Ti-6242 aggregate, shown in Fig. 4, represents a single α grain or a transformed β grain ($\alpha + \beta$ colony). Crystallographic orientations are assigned to the elements in the FE model to be statistically equivalent to those obtained from OIM

scans using a process that involves three main steps delineated as: (a) Orientation assignment using orientation probability assignment method (OPAM); (b) misorientation assignment using misorientation probability assignment method (MPAM); and (c) microtexture assignment using microtexture probability assignment method (MTPAM). The orientation probability assignment methods have been discussed in details in [Deka et al. \(2006\)](#) and [Venkataramani et al. \(2006\)](#). In this model, 70% of the grains are primary α with hcp crystal structure, and the remaining 30% are transformed β grains represented by the homogenized equivalent model. The average simulated stress–strain response for the constant strain rate compression test is plotted in [Fig. 5a](#) and compared with experimental results. Similarly, the volume-averaged simulated plastic strain is plotted as a function of time and compared with results of the compression creep experiment in [Fig. 5b](#). A good agreement is noted between simulation and experimental results for the different test cases.

4. Load shedding and critical microstructural parameters

Experiments on dwell fatigue of Ti-6242 ([Sinha et al., 2006](#)) have shown that large stress concentrations develop with time at the interface of hard and soft grains due to the phenomenon of load shedding. The terms “hard” and “soft” grains in this paper refer to grain strength, which depends on orientation. This should not be confused with the hard and soft slip modes in the transformed β phase corresponding to the slip system deformation resistance as defined in Section 3.2. Load shedding occurs in time dependent or creeping materials due to strength mismatch between neighboring grains that have different orientation of basal planes (see [Fig. 2a](#)) with respect to the loading axis. Grains, which have their $\langle c + a \rangle$ slip active on pyramidal slip systems that have a much higher critical resolved shear stress (CRSS), are designated as hard grains. On the other hand, grains in which the $\langle a \rangle$ type slip on basal or prismatic planes are primarily activated due to their orientation, are designated as soft grains. Time dependent plastic deformation and the total strain evolve rapidly in the soft grains, once the CRSS is reached. Displacement compatibility requirements between a soft and hard grain at the interface cause the local strain in the soft grain near the interface to be lower than that away from it. The plastic strain in this region is high due to lower critical resolved shear stress that causes large number of slip systems to be active. This results in a smaller elastic strain and from [Eq. \(1\)](#), stresses will be lower near the interface in the soft phase. Correspondingly, the compatibility requirement in the hard grain causes the strain near the interface to be higher than that near its center with a lower plastic strain. This gives rise to the high stress concentration near the interface and with increasing creep. The strain increases, and consequently the local stresses also increase as a function of time. Load shedding between the soft and hard oriented grains has been proposed as one of the important factors in dwell fatigue failure. Hence, it is important to understand the load shedding phenomenon in detail and to identify the critical parameters and microstructural conditions, which would contribute to increasing the peak stress due to load shedding. Such a study is also crucial from the viewpoint of design of microstructure as it may provide guidance on microstructural conditions that should be avoided in order to prevent hot spots of stress concentration leading to premature failure. The effect of various microstructural parameters on load shedding is considered in this section.

Load shedding phenomenon due to strength mismatch between hard and soft regions is assumed to depend on (a) mismatch in grain orientation θ_c , (b) misorientation with its neighbor θ_{mis} , (c) mismatch in Schmid factor SF and (d) grain size D. The grain orientation angle θ_c is the angle between the c axis of a grain and the loading axis. The misorientation between two neighboring grains A and B is measured in terms of a rotation axis vector \vec{n} and a misorientation angle θ_{mis} , as described in [Deka et al. \(2006\)](#). The axis \vec{n} represents a common crystallographic lattice or slip direction for both crystal lattices. The misorientation angle θ_{mis} between two neighboring grains is the rotation about \vec{n} required to bring the two crystal lattices into coincidence, and is expressed as

$$\theta = \min \left| \cos^{-1} \left\{ \frac{\text{tr}(\mathbf{g}_A \mathbf{g}_B^{-1} \mathbf{O} - \mathbf{1})}{2} \right\} \right| \tag{14}$$

where \mathbf{g}_A and \mathbf{g}_B are the orientation matrices of grain A and B, respectively and \mathbf{O} is the crystal symmetry operator. In this work the crystal lattices for the grains in θ_{mis} are taken as their “ c ” axes. As seen in [Fig. 6b](#), θ_{mis} represents misorientation between the “ c ” axis of two neighboring grains A and B about the axis \vec{n} . It is measured as the angle between the projections of the two “ c ” axes (dotted) on the plane orthogonal to axis \vec{n} . The Schmid factor, for a slip system is defined as $\text{SF} = \cos \phi \cos \lambda$, where ϕ is the angle between loading axis and the slip plane normal \mathbf{n}_0^z , and λ is the angle between loading axis and the slip direction \mathbf{m}_0^z in the reference configuration. The SF transforms the applied stress to the resolved shear stress on a given slip system.

The dependence of load shedding on these four parameters is studied in detail through creep simulation of a finite element model of a two grain system. The FE model consists of an inner cube representing a primary α hard grain contained in an outer cube representing the softer primary α grain. The loading axis is assumed to coincide with the c axis of the hard grain, for which $\theta_c = 0$, and the corresponding Schmid factor is 0. The orientation of the soft grain is chosen in such a way that a specified Schmid factor on the a_1 basal slip system is achieved. The resulting mismatch in the Schmid factor is equal to the value of Schmid factor of a_1 basal slip of the soft grain. Also, the mismatch in θ_c corresponds to the angle between the loading axis and the c axis of the soft grain. The inner cube (hard grain) is discretized into fine mesh of 1000 tri-linear brick elements while the outer cube (soft grain) has a graded mesh of 6000 elements, as shown in the [Fig. 6a](#). A mesh

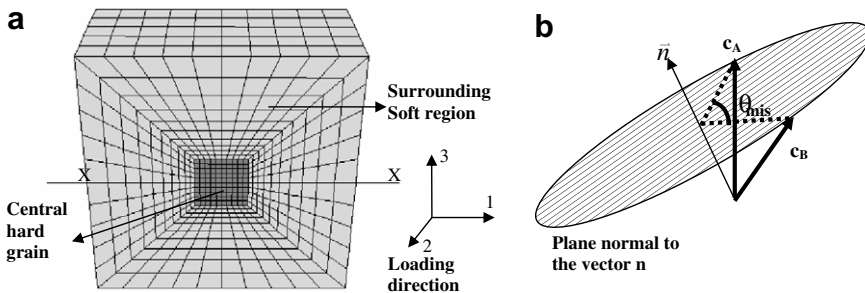


Fig. 6. (a) FE model showing center hard grain which has c -axis aligned with loading axis surrounded by soft grains with basal slip active and loaded in two directions (perpendicular to plane of paper). (b) Schematic showing the misorientation angle θ_{mis} between the crystal lattices corresponding to the “ c ” orientations of two grains A and B.

convergence study is first undertaken with respect to both macroscopic and microscopic response to arrive at this optimal mesh size for the FE model. The two regions in the model can differ in their orientation and size and the steep gradient in stress between the two regions is captured with the refined mesh along the interface.

The creep simulation is carried out at a constant load of 535 MPa, which corresponds to 95% of the yield stress. The \mathbf{a}_1 basal slip is active in the soft region with a Schmid factor of 0.5, since this is expected to give maximum load shedding. The applied load is kept the same for the different cases to identify critical combinations of parameters at a given load. The slip system deformation resistance g_0^2 of individual slip systems for the crystal plasticity simulation is obtained from the Hall–Petch relation in Eq. (10), as explained in Section 3.2. All other crystal plasticity parameters are based on calibrated values in Deka et al. (2006). The loading direction stress (σ_{22}) variation along the section XX in Fig. 6 is plotted after a creep time of 20,000s as a function of the different parameters. The ordinate in these plots shows the maximum value of stress (σ_{22}) in the hard grain near the interface, along the direction of the applied load. This stress is plotted against different variables to identify the critical combination of the parameters that lead to highest stress localization.

In the first case, the effect of θ_{mis} and θ_c on the load shedding response is studied by varying θ_{mis} from 45° and 90° at increments of 15°, while changing θ_c from 30° to 60° at increments of 15°. The Schmid factor is kept constant at 0.45, which gives a little leverage for varying the c axis orientation less than 30° and above 60°, and the characteristic size for both the center and the outer grains is kept as 5 μm . Fig. 7a shows a plot of the maximum stress (σ_{22}) as a function of θ_{mis} for different values of θ_c . The plots remain nearly horizontal implying very little effect of θ_{mis} on σ_{22} . On the other hand, Fig. 7b shows a near linear dependence of σ_{22} on θ_c . The Schmid factor for prismatic and basal systems, other than the \mathbf{a}_1 slip, increases from 0.1 to 0.32 and 0.26 to 0.4 as θ_c increases from 30° to 60°. This is likely a reason for the small increase in stress due to load shedding with increase in θ_c with fixed θ_{mis} .

To study the effect of Schmid factor, the model is adjusted such that the SF of the \mathbf{a}_1 basal slip in the soft outer grain assumes the values 0.425, 0.45, 0.475 and 0.5 respectively. θ_c of the outer region is kept at 50° for all the cases, while the grain size is varied to have the values 5 μm , 25 μm and 50 μm respectively. Fig. 7c shows the variation of σ_{22} with Schmid factor for $\theta_{\text{mis}} = 90^\circ$ for different sizes of the soft grain. There is a significant increase in σ_{22} as the Schmid factor approaches 0.5 especially for the larger grain size. At the smaller grain size, the deformation resistance is considerably higher and there is much less creep leading to very little load shedding. However, the deformation resistance decreases rapidly with increasing grain size to $\sim 50 \mu\text{m}$ and hence large stress concentrations are obtained with increasing Schmid factor. Fig. 7d shows the variation of σ_{22} with increasing soft grain size for different values of SF at a fixed $\theta_{\text{mis}} = 90^\circ$. The size of the inner hard grain is fixed at 5 μm for these plots. Varying the size of the hard grain does not have any appreciable effect on load shedding, as the $\langle c + \mathbf{a} \rangle$ systems, which get activated in the hard grain, have much higher slip system deformation resistance in comparison with the basal systems (~ 2 times). An increase or decrease in slip system deformation resistance of $\langle c + \mathbf{a} \rangle$ system due to size effect relationship does not cause significant change to its high values.

The effect of grain size on load shedding response is studied for various combinations of sizes of hard and soft grains in Venkataramani et al. (2007). It has been shown that the peak stress due to load shedding is governed by the size of the soft grain. Increasing

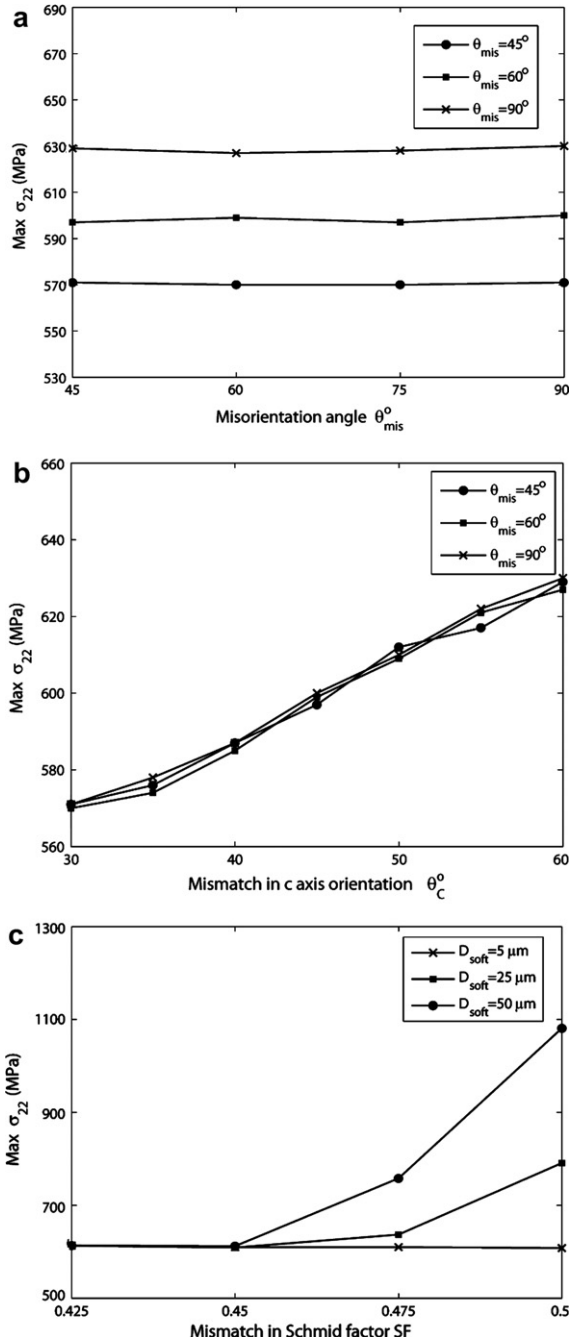


Fig. 7. Variation of peak stress (σ_{22}) in the hard grain with: (a) misorientation angle for different c -axis orientations of the soft grain, (b) mismatch in c -axis orientation between hard and soft grain for different misorientations, (c) mismatch in Schmid factor between hard and soft grain for different grain sizes, and (d) grain size of soft grain for different Schmid factors, at the end of creep time of 20,000s and a stress of 535 MPa.

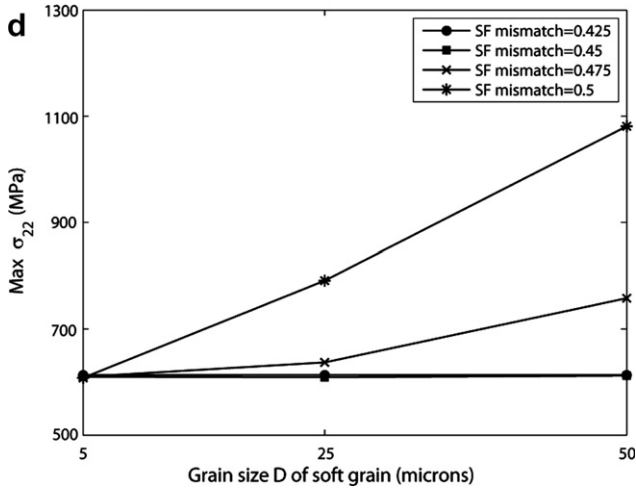


Fig. 7 (continued)

the size of soft grain makes it even softer and thus increases the stress due to load shedding. As seen in Fig. 7c and d, there is no effect of grain size in load shedding response for the lower SFs, i.e. 0.425 and 0.45, but there is a steep increase in the hard grain σ_{22} with increasing grain size at the higher SFs 0.475 and 0.5. This is attributed to the fact that the resolved shear stress in the basal slip system is the highest when the Schmid factor is 0.5 and the slip system deformation resistance is smaller when the grain size is large.

Deformation in the harder grain with the higher strength is predominantly elastic through the loading process and hence an increase in strain in hard grain results in a corresponding increase in stress. From Eq. (4) the creep strain in soft grain is directly proportional to the resolved shear stress τ^α and inversely proportional to the slip system deformation resistance g^α . Hence larger τ^α and smaller g^α will result in higher creep strain with higher load shedding. The resolved shear stress on a particular slip system is directly related to the Schmid factor while the slip system deformation resistance is directly related to grain size. Hence an increase in Schmid factor and an increase in grain size have the effect of increasing the resolved shear stress and decreasing the slip system deformation resistance respectively. This will increase the local creep strain to enhance load shedding as seen in the results of the simulations. The orientation of the ϵ -axis tends to change the Schmid factor and has an indirect effect. However, for the same Schmid factor, a change in the orientation has no effect. The following observations may be summarized from the parametric studies.

- For given ϵ -axis orientation and Schmid factor, change in the misorientation angle θ_{mis} does not have any significant effect on load shedding for any grain size.
- For given Schmid factor and misorientation angle, a change in ϵ -axis orientation mismatch has only a small effect of increasing the stress due to load shedding for any grain size. The increase in stress concentration is due to increase in Schmid factor corresponding to prismatic slip, as the ϵ -axis orientation is changed.

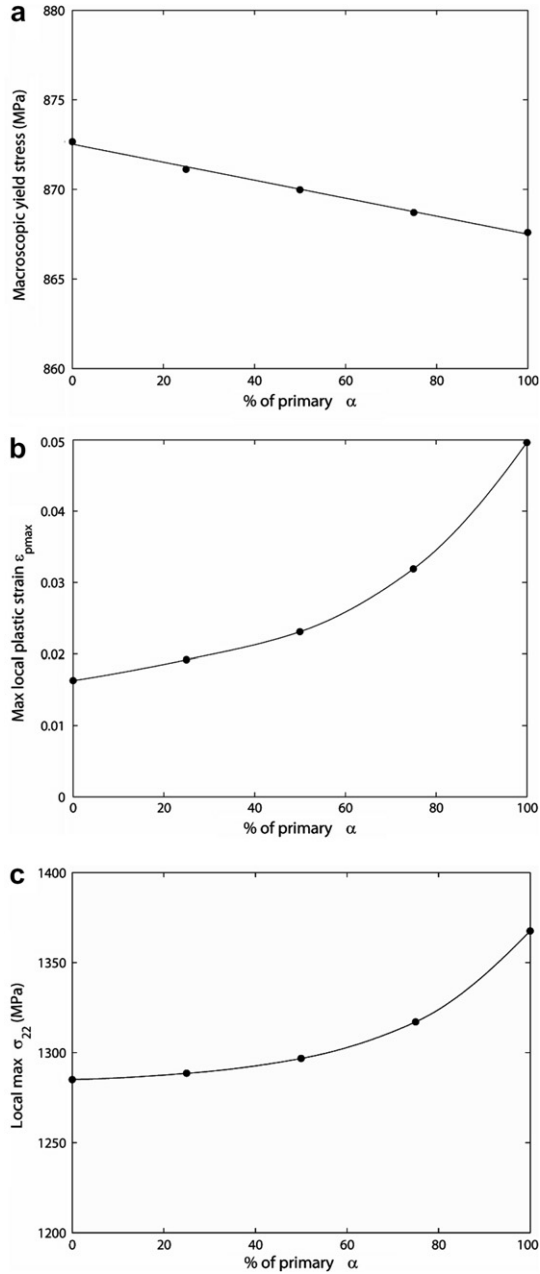


Fig. 8. Variation of (a) yield stress, (b) maximum local plastic strain, and (c) maximum local stress σ_{22} , with different primary α content (%) at the end of 50,000s.

- For given c -axis orientation and misorientation θ_{mis} , an increase in the Schmid factor mismatch will significantly increase load shedding. This effect is accentuated with an increase in the softer grain size.

- The Schmid factor mismatch and grain size are two critical microstructural parameters, which tend to increase stress due to load shedding.

5. Effect of $\alpha - \beta$ composition on creep response

To study the effect of phase proportions a FE model polycrystalline aggregate is constructed and consists of a unit cubic domain that is discretized into 8000 eight-noded tri-linear brick elements (type 7) in the commercial finite element code **MARC** (2005). Each element in the FE model represents a grain in a polycrystalline aggregate. Texture assignment to the FE model involves three main steps delineated in [Deka et al. \(2006\)](#), [Venkataramani et al. \(2006\)](#) as: (a) Orientation assignment using orientation probability assignment method (OPAM); (b) misorientation assignment using misorientation probability assignment method (MPAM); and (c) microtexture assignment using microtexture probability assignment method (MTPAM). The probability assignment methods invoke iterations to statistically match experimentally observed orientation distributions as detailed in [Deka et al. \(2006\)](#) and [Venkataramani et al. \(2006\)](#). The effect of proportion of phases is studied by varying the volume fraction in the primary α phase from 0% to 100%, while keeping the volume fraction of hcp and bcc phases in the transformed β region fixed at 88% and 12% respectively. Constant strain rate and creep simulations are carried out for the polycrystalline FE model with various phase proportions.

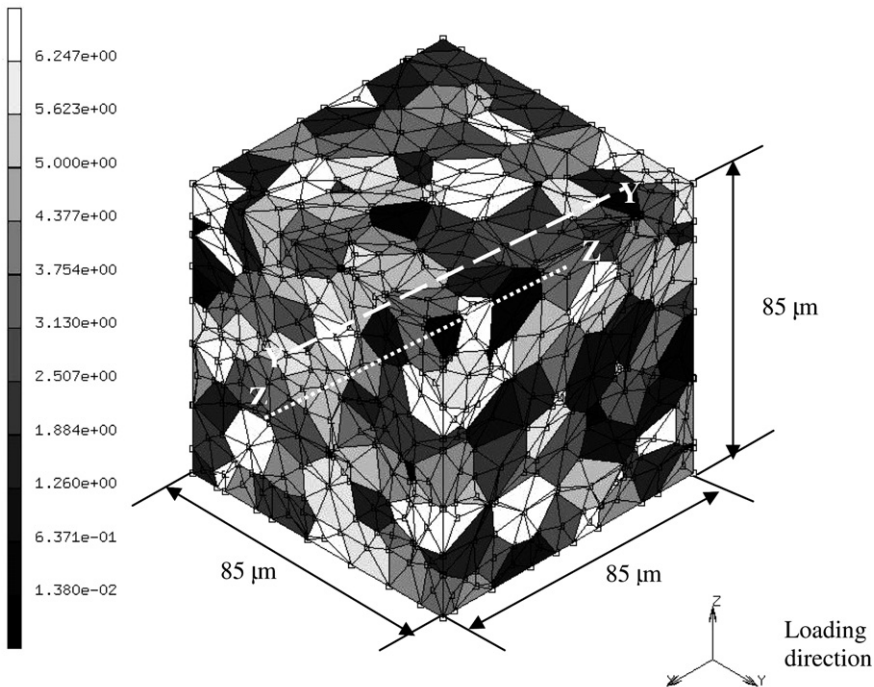


Fig. 9. A 3D statistically equivalent microstructure model meshed with 3D tetrahedron elements showing contour of orientation distribution (radians).

Fig. 8a shows the variation of macroscopic yield stress for various volume fractions of the primary α phase. With increase in the α phase concentration from 0% to 100%, the yield stress reduces almost linearly. A higher yield stress is observed for higher fraction of the transformed β phase. Correspondingly the maximum creep strain at a time of 50,000 s increases with increasing primary α phase in Fig. 8b, which is consistent with the experimental observations of less dwell debit with a lean primary α content (Kassner et al., 1999). The higher plastic strain accumulation has the effect of increasing load shedding between hard and soft oriented grains thus resulting in high stress concentrations as seen in the plot of peak stress variation with composition in Fig. 8c. Consequently, there is a higher stress concentration in pure primary α in comparison with microstructures with both phases present. Hence, a bimodal microstructure is more desirable than just pure primary α phase.

6. Realistic microstructure modeling of grain morphology

Grain morphologies in real polycrystalline microstructures have arbitrary distributions of shapes and sizes, which are quite different from the uniform cubic grains assumed in the previous examples. The grain irregularities introduce additional complexity in the microstructural stress and strain evolution. A 3D microstructure model with statistically equivalent microstructural morphological and crystallographic characteristics of a real polycrystalline material is therefore analyzed in this section.

In the recent years, there have been significant advances in reconstruction and simulation of 3D polycrystalline microstructures based on information obtained from a dual beam focused ion beam-scanning electron microscope system. This system is able to acquire 3D orientation or electron backscatter diffraction (EBSD) data from a series of material cross sections. This information has been successfully used in Bhandari et al. (submitted for publication) for automatic segmentation of individual grains from the image and translated into a 3D mesh used subsequently in FE analysis. Through a multitude of data sets the intrinsic distributions of microstructural parameters can be captured and accurately represented through 3D microstructure reconstruction. Computational tools have been developed in Bhandari et al. (submitted for publication, in press) and Groeber et al. (2006, submitted for publication-a, submitted for publication-b) to create simulated microstructures that are statistically equivalent to the measured structure. This methodology first uses 3D characterization to generate distribution functions of various microstructural parameters. Subsequently, a constrained Voronoi tessellation of the 3D region is executed, where the tessellation process is biased by statistics of the generated distributions. Crystallographic orientations are subsequently assigned to the grains using the OPAM, MPAM and MTPAM algorithms for orientation, misorientation and microtexture distributions respectively mentioned in Section 3. Such a simulated microstructure is generated and meshed into a 3D FE mesh in the present study to understand the importance of Schmid factor and grain size on load shedding in real microstructures.

The FE model, shown in Fig. 9, has a large microtextured region of grains with their c -axis nearly aligned with loading axis. The microtextured regions have been identified in Sinha et al. (2006) as regions of possible crack initiation. The polycrystalline model has dimensions $85 \mu\text{m} \times 85 \mu\text{m} \times 85 \mu\text{m}$, and consists of 500 grains that have orientation, misorientation, microtexture and size distributions, statistically equivalent to those observed in OIM scans of a sample of Ti-6242. The model has 70% primary α and 30% transformed β grains. The slip system deformation resistance g^z of individual slip systems

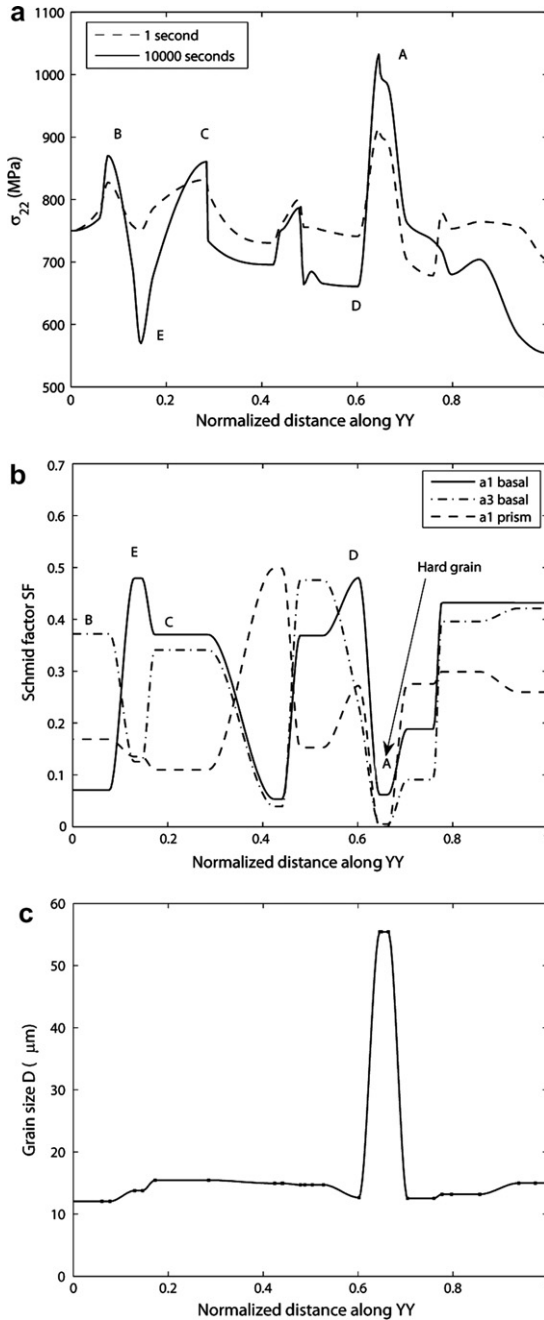


Fig. 10. Distribution of local variables: (a) loading direction stress (σ_{22}), (b) three prominent Schmid factors for the a_1 basal, a_3 basal and a_1 prism slip systems, (c) grain size, and (d) c -axis orientation, along a section YY parallel to the x -axis at the end of creep time of 1s and 10,000s and a stress level of 800 MPa.

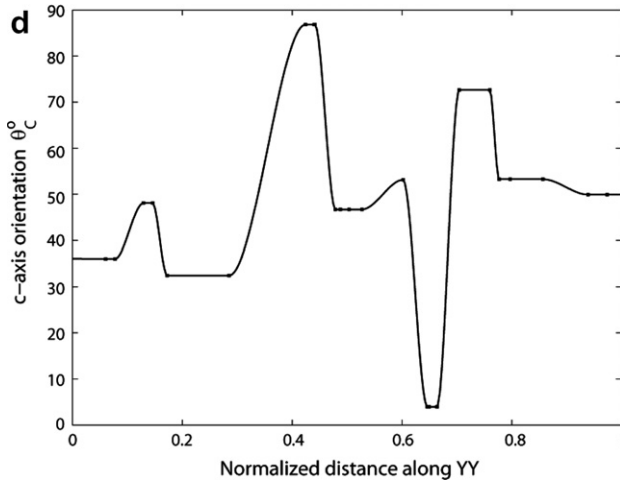


Fig. 10 (continued)

for the crystal plasticity simulation is obtained from the size effect relationship Eq. (10), based on the grain size. All other crystal plasticity parameters are those that have been calibrated in [Deka et al. \(2006\)](#). The 3D FE model is used to understand the significance of size, Schmid factor and c -axis orientation on the load shedding response between hard and soft grains. The microstructural creep response is studied at the end of 1 s and 10,000 s, simulated for an applied load of 800 MPa in the ‘ y ’ direction shown in [Fig. 9](#). Minimum boundary constraints to prevent rigid body rotation are employed to the model.

The distribution of local stress σ_{22} in the loading direction, Schmid factor (SF), grain size D and the c -axis orientation θ_c is plotted along two representative sections YY and ZZ in [Figs. 10 and 11](#) respectively. The sections are parallel to the x -axis and are at normalized (y, z) coordinates (0.3, 0.2) for section YY and (0.1, 0.1) for section ZZ respectively, as seen in [Fig. 9](#). Since the three basal and prismatic slip systems are the easiest to slip due to low g^z , the values of the SFs for these six slip systems are important. The distribution of the SFs for each of the slip systems along the sections YY and ZZ are examined. The three slip systems, which have the higher SFs are chosen and plotted in [Fig. 10b](#). For the section YY, the SFs of the a_1 basal, a_3 basal and a_1 prism slip systems are prominent, while for the section ZZ the SFs of all the three basal slip systems are prominent.

As seen in [Fig. 10a](#), the distribution of stress along YY, which passes through a micro-textured hard region, is highly non-uniform owing to the mismatch in strength between neighboring grains. The stress peaks are at **A**, **B** and **C** while the valleys are at **D** and **E**. A comparison of the stress distribution along the section at the end of 1 s and 10,000 s shows that the stress peaks corresponding to the points **A**, **B** and **C** rise with time while those at **D** and **E** drop with time as a consequence of creep and load shedding from grains at **D** and **E** on to the corresponding grains at **A**, **B** or **C**. From the plots of the prominent Schmid factor distributions in [Fig. 10b](#), it is seen that point **A** corresponds to a hard grain with low Schmid factors on all prominent slip systems that is adjacent to a grain **D** with a high Schmid factor of 0.5 on the a_1 basal slip system. This causes a large mismatch

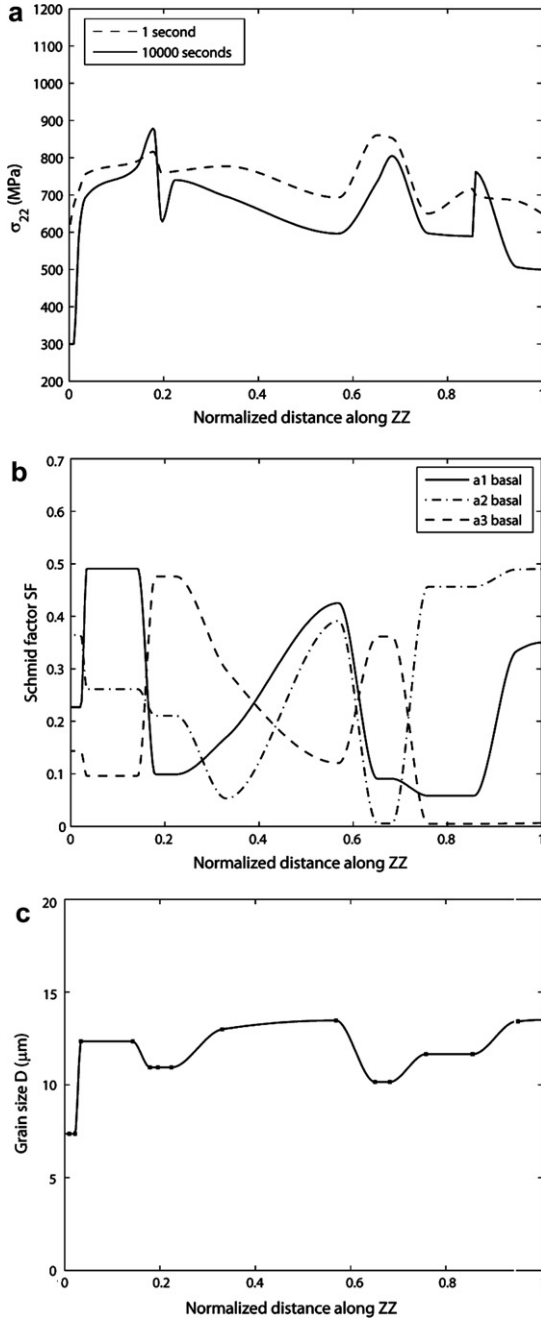


Fig. 11. Distribution of local variables: (a) loading direction stress (σ_{22}), (b) three prominent Schmid factors for a_1 , a_2 and a_3 basal slip systems, (c) grain size, and (d) c -axis orientation, along a section ZZ parallel to the x -axis at the end of creep time of 1s and 10,000s and a stress level of 800 MPa.

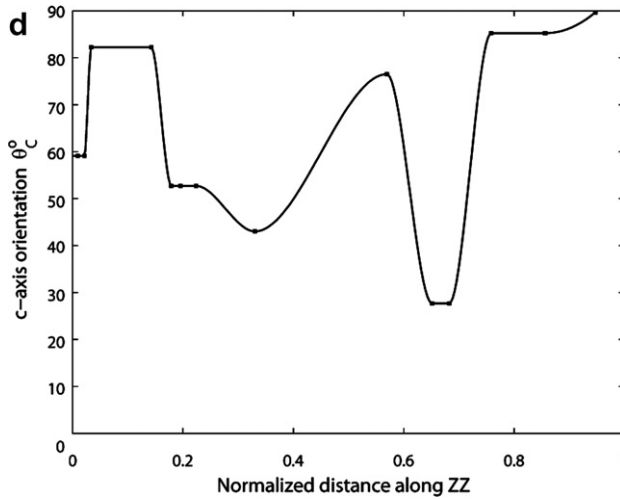


Fig. 11 (continued)

in Schmid factor between the two grains and increases load shedding from the soft grain at **D** to the hard grain at **A**. The point **B** has a_3 basal SF of around 0.4 and **C** has an a_1 basal SF of around 0.4. Both **B** and **C** are adjacent to a grain at **E** with a high a_1 basal SF of nearly 0.5. This mismatch also results in load shedding between grains having moderate to high $\langle a \rangle$ slip activity. It is however not as pronounced as grains at **A** where load shedding is between $\langle a \rangle$ and $\langle c + a \rangle$ oriented grains. While the size of the hard grain at **A** is greater than the surroundings, as seen in Fig. 10c, the effect of size (D) dependent lowering of g_0^z in Eq. (10) is not significant enough in comparison with the high \bar{g}_0^z value of the hard grain. The plots along the section ZZ in Fig. 11 show that there is no steep increase in the stress with time in comparison with Fig. 10a. It can also be seen from Fig. 11a that there is no steep gradient in the stress σ_{22} due to the absence of $\langle c + a \rangle$ oriented hard grains. Along the entire section at least one of the prominent SFs is high (0.4–0.5). In other words, the section ZZ consists of soft or moderately soft grains and hence only moderate stress variation is observed in this section. From these plots it can be concluded that a mismatch in Schmid factor results in load shedding between the grains that is predominant when there is a hard grain with $\langle c + a \rangle$ slip activity. This is consistent with earlier observations on Schmid factor and load shedding in Section 4. With the realistic 3D microstructure modeling, the effect of grain shape and irregularity of grain interfaces in stress and strain concentration can be accounted for in addition to texture and size effects. Such analysis, accounting for various microstructural parameters is needed for establishing robust crack initiation criterion in polycrystalline Ti-6242 subjected to dwell fatigue.

7. Conclusions

This paper presents the results of an important parametric study that is necessary for identifying critical microstructural parameters that influence creep induced load shedding leading to crack initiation in polycrystalline Ti-6242 microstructure. A size and rate depen-

dent, anisotropic elastic–crystal plastic material model is developed and is incorporated in a finite element model of the Ti-6242 alloy. The model accounts for various microstructural characteristics that are needed for the parametric study and sensitivity analysis of polycrystalline materials with respect to creep and load shedding. The effect of four microstructural parameters, viz. mismatch in c -axis orientation, misorientation, Schmid factor mismatch and grain size, on load shedding between hard and soft oriented grain is studied. The ranges of the values of the variables are chosen to cover all possible combinations in the microstructure. From the results of the study it is concluded that load shedding is pronounced in regions of hard oriented grains surrounded by large sized soft oriented grains with high (~ 0.5) basal or prismatic Schmid factor. It is found that c -axis orientation mismatch and misorientation do not play dominant roles in causing stress concentration due to load shedding. However, they may indirectly determine the Schmid factor of a grain. Also, while load shedding strongly depends on the size of soft grain, the size of hard grain has virtually no effect on this response.

The strength and creep response of polycrystalline Ti-6242 is also influenced by the proportion of phases. It is shown that as the primary α content increases, the yield strength decreases while the local creep strain and stress (σ_{22}) increase. This is in agreement with experimental observation of low dwell debit for lean primary α content. A microstructure that has a higher proportion of transformed β has a higher yield and a lower plastic strain accumulation and hence is more resistant to creep and dwell induced load shedding.

A 3D polycrystalline model is simulated by a constrained Voronoi tessellation method to match the statistical distribution of grain size, texture, orientation and misorientation of the Ti-6242 microstructure. The 3D FE model accounts for grain shape complexities in addition to texture and size effects and serves as a useful tool for the identification of local hot spots and crack initiation sites in a real microstructure. The evolution of stress with creep along different sections of the microstructure is studied and analyzed against local microstructural characteristics. A mismatch in Schmid factor results in load shedding between the grains that is predominant when there is a hard grain with $\langle c + a \rangle$ slip activity. No stress gradient is observed in the section with no hard grain orientation. This study emphasizes the importance of Schmid factor and realistic representation of grain size and shape on load shedding. This work helps to identify critical parameters, which need to be avoided to minimize stress concentrations in the microstructure and prevent early crack initiation in Ti-6242 under creep and dwell fatigue.

Acknowledgements

The authors are grateful to Professors Jim Williams, Mike Mills, Stan Rokhlin and Dr. Vikas Sinha for providing guidance and the experimental data. This work has been supported by the Federal Aviation Administration through grant No. DTFA03-01-C-0019 (Program Director: Dr. Joe Wilson). This support is gratefully acknowledged. The authors gratefully acknowledge the software support provided by Dr. Sanjay Choudhry and Dr. Shiva Padmanabhan of MSC MARC. The authors acknowledge the insightful suggestions of Drs. A. Woodfield, A. Chatterjee, J. Hall, J. Schirra and M. Savage on various aspects of this work. Computer support by the Ohio Supercomputer Center through grant # PAS813-2 is also acknowledged.

References

- Bache, M.R., 2003. A review of dwell sensitive fatigue in titanium alloy: the role of microstructure, texture and operating conditions. *Int. J. Fatigue* 125, 241.
- Bhandari, Y., Groeber, M., Ghosh, S., submitted for publication. CAD based reconstruction of three dimensional polycrystalline microstructures from fib generated serial sections. *Comput. Aid. Des.*
- Bhandari, Y., Sarkar S., Groeber M., Uchic, M.D., Dimiduk, D.M., Ghosh, S., in press. 3D polycrystalline microstructure reconstruction from FIB generated serial sections for FE Analysis. *Comput. Mater. Sci.*
- Cao, G., Fu, L., Lin, J., Zhang, Y., Chen, C., 2000. The relationships of microstructure and properties of a fully lamellar Ti–Al alloy. *Intermetallics* 8, 647.
- Chu, H.P., 1970. Room temperature creep and stress relaxation of a titanium alloy (Ti alloy tension creep tests at room temperature, determining strength for correlation with stress relaxation). *J. Mater.* 5, 633.
- Deka, D., Joseph, D.S., Ghosh, S., Mills, M.J., 2006. Crystal plasticity modeling of deformation and creep in polycrystalline Ti-6242. *Metall. Mater. Trans. A* 37A, 1371.
- Eshelby, J.D., 1963. The distribution of dislocations in an elliptical glide zone. *Phys. Status Solidi* 3, 2057.
- Froes, F.H. (Ed.), 1998. *Non-Aerospace Applications of Titanium*. TMS, Warrendale, PA.
- Goh, C.-H., Neu, R.W., McDowell, D.L., 2003. Crystallographic plasticity in fretting of Ti–6Al–4V. *Int. J. Plast.* 19 (10), 1627.
- Groeber, M., Uchic, M.D., Dimiduk, D.M., Bhandari, Y., Ghosh, S., 2006. Reconstruction and characterization of 3D microstructures: an unbiased description of grain morphology. In: *Multi-scale Materials Modeling Conference Proceedings, Symposium 4*, Freiburg, Germany.
- Groeber, M., Ghosh, S., Uchic, M.D., Dimiduk, D.M., submitted for publication-a. A framework for automated analysis and representation of 3D polycrystalline microstructures, Part 1: statistical characterization, *Acta Mater.*
- Groeber, M., Ghosh, S., Uchic, M.D., Dimiduk, D.M., submitted for publication-b. A framework for automated analysis and representation of 3D polycrystalline microstructures, Part 2: synthetic structure generation, *Acta Mater.*
- Hall, E.O., 1951. The deformation and ageing of mild steel III, discussion of results. *Proc. Phys. Soc. B* 6, 747.
- Harren, S., Lowe, T.C., Asaro, R.J., Needleman, A., 1989. Analysis of large strain shear in rate dependent face centered cubic polycrystals: correlation of micro- and macro-mechanics. *Philos. Trans. R. Soc. London A* 238, 443.
- Hasija, V., Ghosh, S., Mills, M.J., Joseph, D.S., 2003. Deformation and creep modeling in polycrystalline Ti–6Al alloys. *Acta Mater.* 51, 4533.
- Imam, M.A., Gilmore, C.M., 1979. Room temperature creep of Ti–6Al–4V. *Metall. Trans. A* 10A, 419.
- Kalidindi, S.R., Bronkhorst, C.A., Anand, L., 1992. Crystallographic texture evolution in bulk deformation processing of FCC metals. *J. Mech. Phys. Solids* 40, 537.
- Kassner, M.E., Kosaka, Y., Hall, J.A., 1999. Low-cycle dwell-time fatigue in Ti-6242. *Metall. Trans. A* 30A, 2383.
- Kothari, M., Anand, L., 1998. Elasto-viscoplastic constitutive equations for polycrystalline metals: application to tantalum. *J. Mech. Phys. Solids* 46, 51.
- Li, J., Chou, Y., 1970. The role of dislocations in the flow stress grain size relationships. *Metall. Trans.* 3, 1145.
- Maruyama, K., Yamada, N., Sato, H., 2001. Effects of lamellar spacing on mechanical properties of fully lamellar Ti–39.4 mol%Al alloy. *Mater. Sci. Eng. A* 319–321, 360.
- Miller, W.H., Chen, R.T., Starke, E.A., 1987. Microstructure, creep, and tensile deformation in Ti–6Al–2Nb–1Ta–0.8 Mo. *Metall. Trans. A* 18A, 1451.
- MSC-MARC Reference Manuals, 2005, MSC, Software Corporation.
- Neeraj, T., Savage, M.F., Tatalovich, J., Kovarik, L., Hayes, R.W., Mills, M.J., 2005. Observation of tension compression asymmetry in α and α/β titanium alloys. *Philos. Mag.* 85 (2–3), 279.
- Norfleet, D., The Ohio State University, Columbus, OH, unpublished research, 2005.
- Odegard, B.C., Thompson, A.W., 1974. Low temperature creep of Ti–6 Al–4V. *Metall. Trans.* 5, 1207.
- Petch, N.J., 1953. The cleavage strength of polycrystals. *J. Iron Steel Inst. London* 173, 25.
- Savage, M.F., 2000. *Microstructural and Mechanistic Study of Low Temperature Creep and Dwell Fatigue in Single Colony alpha/beta Titanium Alloys*, Ph.D. Dissertation, OSU, Columbus, OH.
- Semiatin, S.L., Bieler, T.R., 2001. The effect of alpha platelet thickness on plastic flow during hot working of Ti–6Al–4V with a transformed microstructure. *Acta Mater.* 49, 3565.

- Sinha, V., Mills, M.J., Williams, J.C., 2004. Understanding the contributions of normal-fatigue and static loading to the dwell fatigue in a near-alpha titanium alloy. *Metall Mater. Trans. A* 35A, 3141.
- Sinha, V., Spowart, J.E., Mills, M.J., Williams, J.C., 2006. Observations on the faceted initiation site in the dwell-fatigue tested Ti-6242 alloy: crystallographic orientation and size effects. *Metall. Mater. Trans. A* 37A, 1507.
- Suri, S., Viswanathan, G.B., Neeraj, T., Hou, D.H., Mills, M.J., 1999. Room temperature deformation and mechanisms of slip transmission in oriented single-colony crystals of an alpha/beta titanium alloy. *Acta Mater.* 47 (3), 1019.
- Venkataramani, G., Deka, D., Ghosh, S., 2006. Crystal Plasticity based FE model for understanding microstructural effects on creep and dwell fatigue in Ti-6242. *J. Eng. Mater. Tech. ASME* 128, 356.
- Venkataramani, G., Ghosh, S., Mills, M.J., 2007. A size dependent crystal plasticity finite element model for creep and load-shedding in polycrystalline Titanium alloys. *Acta Mater* 55, 3971.
- Williams, J.C., Baggerly, R.G., Paton, N.E., 2002. Deformation behavior of HCP Ti-Al alloy single crystals. *Metall. Mater. Trans. A* 33, 837.